

Gravitational lensing by the supermassive black hole in the center of M31

V. Bozza^{1,2}, S. Calchi Novati^{1,2} and L. Mancini^{1,2}

¹*Dipartimento di Fisica “E.R. Caianiello”, Università di Salerno, via S. Allende, Baronissi (SA), Italy.*

²*Istituto Nazionale di Fisica Nucleare, Sezione di Napoli, Italy.*

ABSTRACT

We examine the possibility of observing gravitational lensing in the weak deflection regime by the supermassive black hole in the center of the galaxy M31. This black hole is significantly more massive than the black hole in the center of our Galaxy qualifying itself as a more effective lens. However, it is also more distant and the candidate stellar sources appear consequently fainter. As potential sources we separately consider stars belonging to the bulge, to the disk, to the triple nucleus formed by P1+P2 and by the recently discovered inner cluster P3. We calculate the number of simultaneously lensed stars at a given time as a function of the threshold magnitude required for the secondary image. For observations in the K-band we find 1.4 expected stars having secondary images brighter than $K = 24$ and 182 brighter than $K = 30$. For observations in the V-band we expect 1.3 secondary images brighter than $V = 27$ and 271 brighter than $V = 33$. The bulge stars have the highest chance to be lensed by the supermassive black hole, whereas the disk and the composite nucleus stars contribute by 10% each. The typical angular separation of the secondary images from the black hole range from 1 mas to $0.1''$. For each population we also show the distribution of the lensed sources as a function of their distance and absolute magnitude, the expected angular positions and velocities of the generated secondary images, the rate and the typical duration of the lensing events.

Subject headings: Gravitational lensing — Black hole physics — galaxies: individual (M31) — galaxies: nuclei

1. Introduction

As soon as the evidence of a supermassive black hole in the center of the Milky Way (identified with the radio source Sgr A*) became overwhelming, the scientific community

started to investigate its ability of acting as a gravitational lens for background stellar sources. The first work by Wardle & Yusuf-Zadeh (1992) considered lensing of sources in the immediate environment of Sgr A* and showed that the background sky should appear slightly depleted by a lensing effect. They suggested the possibility that gravitational lensing could be strong enough to generate an observable secondary image for several stars at a given time. More precise estimates by Jaroszyński (1998), Alexander & Sternberg (1999), and Chanamé et al. (2001), point out that about 10 stars belonging to the Galactic bulge should give rise to secondary images with $K < 23$ at a given time. Deep and high resolution images in the near infrared of the Galactic center are being obtained by several advanced observatories such as Keck, VLT, and Gemini North. The progress registered by these observations encourages to search for signatures of lensing effects by Sgr A*. For example, identifying the two images of a background source (Alexander 2001), or measuring the astrometric shift of the background stars due to gravitational lensing (Nusser & Broadhurst 2004), could help to determine the position of Sgr A* very accurately. Enhanced microlensing caused by black holes surrounding Sgr A* has also been considered (Alexander & Loeb 2001; Chanamé et al. 2001). A fascinating possibility is offered by stars orbiting very close to Sgr A*, which have now been followed very accurately across several years (Eckart & Genzel 1997; Genzel et al. 1996; Ghez et al. 1998; Eckart et al. 2002; Schödel et al. 2002, 2003; Ghez et al. 2003, 2005; Weinberg et al. 2005; Eisenhauer et al. 2005; Paumard et al. 2006; Reid et al. 2006). In fact, the precise knowledge of the position of the source allows to predict the time, the position and the brightness of the secondary image (De Paolis et al. 2003; Bozza & Mancini 2004, 2005).

Meanwhile, our knowledge about the central regions of the Andromeda galaxy (M31) has grown considerably. Kent (1989) has provided a detailed brightness and density profile for the bulge and the disk of M31, which is still the reference for present works. Lauer et al. (1993) discovered that the nucleus of M31 is actually constituted by two components, which they called P1 and P2. King et al. (1995) noticed that P2 is much brighter than P1 in the ultraviolet. Then Tremaine (1995) hypothesized that P1 and P2 are actually parts of the same eccentric disk orbiting a supermassive black hole, with P1 being formed by stars at the apocenter and P2 being formed by stars at the pericenter. Later on, Bender et al. (2005) discovered a bright cluster of young stars (named P3) embedded within P2. They also managed to give the most precise estimate for the mass of the central black hole of M31, $M = 1.4^{+0.9}_{-0.3} \times 10^8 M_{\odot}$. Recently, Demarque & Virani (2007) have cast doubt on the hypothesis that the P3 cluster is made of young stars of spectral class A5 – B5, proposing that it is actually made of old stars. On the other hand, Chang et al. (2007) have supported the young-stars hypothesis suggesting a mechanism for the refuelling of gas in the neighborhood of the central black hole.

It is very interesting to note that the supermassive black hole in the center of M31 is nearly two orders of magnitudes heavier than the black hole in our Galaxy, estimated to $3.6 \times 10^6 M_{\odot}$ by Eisenhauer et al. (2005). From the lensing point of view, the greater distance of M31 with respect to Sgr A* is therefore partly compensated by the larger mass of its central black hole. This motivates a deep investigation of the probability of having stellar sources lensed by the supermassive black hole in M31.

Gravitational lensing effects have been successfully employed in several contexts as a tool to study the structure of galaxies, large-scale structures and cosmological parameters (Kochanek et al. 2004). As we will show in this paper, it is not unlikely that gravitational lensing by the supermassive black hole in M31 will follow the wake of its ancestors. With a conspicuous number of events it will be possible to undertake a precise reconstruction of the mass distribution in the inner core of M31. Gravitational lensing would then provide an independent and unbiased method to be crossed with other investigation methods such as object counting, spectroscopic or proper motion measurements and so on. Indeed the study of the physics of the core of M31 would greatly benefit from these new data, which will help to understand the physics of the stellar environment of supermassive black holes and possibly shed light on the true origin of these enigmatic objects.

In this paper, we shall exploit the present knowledge of the bulge and the disk populations in M31 to calculate the expected number of simultaneously lensed sources for a given threshold magnitude in either the *K*-band or the *V*-band. We will also consider sources belonging to the central clusters, modelling P1 and P2 as components of a single eccentric system and P3 as a separate inner stellar cluster surrounding the central black hole. For each of the four populations (disk, bulge, P1+P2, P3), we shall present several probability distributions characterizing the properties of the lensing events. The paper is structured as follows: in § 2 we indicate our reference models for the source populations and describe their features. In § 3 we review some basics on gravitational lensing, with particular reference to the black hole in M31. In § 4 we present our estimates for the number of lensed sources at any given time for a given threshold magnitude of the secondary image. In § 5 we examine the contribution of sources of different magnitude to the total number of events. In § 6 we give the distribution of events as a function of the source distance. In § 7 we show the distribution of the angular positions of the images. In § 8 we present the distribution of their apparent angular velocities. In § 9 we estimate the rate and the average duration of the lensing events. In § 10 we discuss some issues concerning the identification of the lensing events. § 11 contains the conclusions.

2. Source populations

Our aim is to calculate lensing probabilities for four different populations of stellar sources around the supermassive black hole in the center of M31, namely P3, P1+P2, the bulge and the disk. We therefore introduce specific models for each population containing information on their spatial distribution, kinematic properties and luminosity function, which are the necessary elements for the calculation of the lensing probabilities to be treated in the succeeding sections.

For all populations, we choose to normalize the spatial distribution f_{P_j} to unity, so that the quantity $f_{P_j}(x, y, z)dxdydz$ represents the probability of finding a single star of the population P_j in the space element $dxdydz$.

We shall present gravitational lensing probability estimates for hypothetic observation programs in the V -band ($\sim 0.55 \mu\text{m}$) or in the K -band ($\sim 2.2 \mu\text{m}$). The K -band presents some considerable advantages for this kind of research, since the interstellar extinction is lower in the near infrared than in the visible. In fact, in the K -band the total average extinction (M31 + our Galaxy) is $A_K = 0.1$ (Olsen et al. 2006), whereas in the V -band we have $A_V = 0.31$. The latter value can be deduced by adding the intrinsic extinction of the M31 galaxy $A_{V,\text{int}} = 0.12$ (half the value given by Han 1989, since our sources are close to the center of M31) to the foreground extinction $A_{V,\text{ext}} = 0.19$ (Schlegel et al. 1998). Moreover, large ground-based telescopes are optimized for interferometry in the infrared bands. In the most powerful configuration, they can reach resolutions of order the mas. Such capability would be very precious for the detection of secondary images generated in gravitational lensing events. Even the forthcoming *James Webb Space Telescope (JWST)* is designed to carry instruments for deep infrared imaging (Gardner et al. 2006). On the other hand, the V -band is less affected by background noise. Furthermore, at the diffraction limit, the V -band enjoys a resolution 4 times better than the K -band, though large interferometers operating in the visible bands are still far to come.

In any case, by comparing the results in the two bands we get a much deeper understanding on the source selection operated by the gravitational lensing phenomenon. Since the stellar populations have different luminosity functions in the two bands, all gravitational lensing distributions look different, with some features exalted or depressed. This also allows a quick double-check of our results.

On the basis of this choice, we need the luminosity functions of each source population both in the K -band and in the V -band. In the K -band, this function will be expressed as $n_{P_j}(M_K)$, defined so that $n_{P_j}(M_K)dM_K$ represents the number of stars belonging to the population P_j with absolute magnitude in the range $[M_K, M_K + dM_K]$. The total number

of stars belonging to the population P_j is recovered after integration on all magnitudes

$$N_{P_j}^{\text{tot}} = \int n_{P_j}(M_K) dM_K. \quad (1)$$

The same definitions hold for the V -band, with the obvious changes in the notation. The following subsections explain the construction of the luminosity functions and the choice of the spatial distribution for each stellar population.

2.1. P3

The cluster P3 was discovered by Bender et al. (2005) through spectroscopic observations using the *Hubble Space Telescope (HST)*. Although this cluster is embedded within P2 (see § 2.2), it is characterized by a distinct stellar population and different kinematic properties, strongly indicating that it must be considered as a separate entity.

The characteristics of P3 are consistent with the hypothesis of a circular disk of stars in Keplerian rotation around the central supermassive black hole. In particular, Bender et al. (2005) used two models to fit the spectroscopic observations: an exponential flat disk and a Schwarzschild (1979) triaxial model. The best fits were obtained with the flat disk or a thin Schwarzschild model, with axial ratio 0.26. As a reasonable synthesis of the models explored by Bender et al. (2005), we choose a classical thick-disk spatial distribution

$$f_{P3}(x, y, z) = \frac{1}{4\pi r_{P3}^2 z_{P3}} \exp \left[-\frac{\sqrt{x^2 + y^2}}{r_{P3}} \right] \text{sech}^2 \left[\frac{z}{z_{P3}} \right] \quad (2)$$

with the disk scale being $r_{P3} = 0.8$ pc and thickness $z_{P3} = 0.1$ pc. The inclination of the disk relative to the line of sight is $i_{P3} = 55^\circ$, similar to that of the system P1+P2.

The rotation curve of P3 is symmetric around its center, reaching a rotation velocity $v_{P3} = 618$ km s⁻¹ and dispersion $\sigma_{P3} = 674$ km s⁻¹.

For the luminosity function of P3 we have followed Bender et al. (2005), who use the synthetic color-magnitude diagram generated by the program IAC-STAR by Aparicio & Gallart (2004). We have run this program with the same parameters, accepting the hypothesis that P3 was generated by a single starburst that occurred 200 Myr ago in a gas cloud with solar metallicity (see Demarque & Virani 2007 for an alternative proposal). We adopt a Kroupa et al. (1993) initial mass function. The algorithm has returned us 10^5 stars with $M_K < 6$. Such a number turns out to be insufficient for a substantial covering of the giant stars branches. We have thus generated a second sample of 10^5 stars with $M_K < 1$ and

combined the two samples with appropriate weights. The two samples are shown together in two different color-magnitude diagrams in Figure 1. The cut-off at $M_K = 6$ does not translate into a sharp cut-off in the V -band. However, the sample is completely unaffected for $M_V < 8$, which we take as our cut-off in the luminosity function in the V -band. It is important to stress that gravitational-lensing observations select very bright sources with much higher probability than faint ones. For this reason, we do not pay much attention to the completeness of our simulated samples of stars on the low-luminosity side. In the same way, issues concerning the lower cutoff of the initial mass function are not relevant for us. All gravitational lensing probabilities are practically insensitive to changes in the source distribution function at low luminosities. This statement is also supported *a posteriori* by the distributions presented in § 5.

Note that the red giant branch (RGB) lies at almost fixed magnitude in the V -band, whereas it spans 6 magnitudes in the K -band up to the tip.

The normalization of our sample of P3 stars has been performed introducing a factor N multiplying the total number of stars. The value of N has been deduced by comparing the total magnitude in the V -band of our artificial set with the total magnitude of P3 as deduced by Bender et al. (2005), being $M_{V,P3} = -5.7$.

$$M_{V,P3} = -2.5 \log_{10} N - 2.5 \log_{10} M_{V,P3\text{-sample}}, \quad (3)$$

where $M_{V,P3\text{-sample}}$ is the unnormalized absolute magnitude of our combined sample. Also this normalization procedure on the number of stars deduced by the total luminosity is largely insensitive to the abundance of low-luminosity stars.

Finally, the same set of stars has been used to build a binned luminosity function in the K -band and in the V -band, normalized in the way just described. The values of these binned functions are shown in Tables 1 and 2, together with those of the other source populations, to be discussed in the succeeding sections.

The different orientation of the RGB in the V -band and in the K -band is reflected in the luminosity function, which is zero in the V -band up to $M_V \simeq -2.75$, whereas it is already non-zero in the K -band at $M_K \simeq -9.75$. The K -band luminosity function clearly shows a red clump at $M_K \simeq -3.75$, which is not as clear in the V -band, where it overlaps the stars at the turn-off point (TOP) of the main sequence (MS). It is worth noting that the real number of stars in P3 should be of order a few thousands, whereas we have simulated 2×10^5 stars in order to have a statistically significant sample.

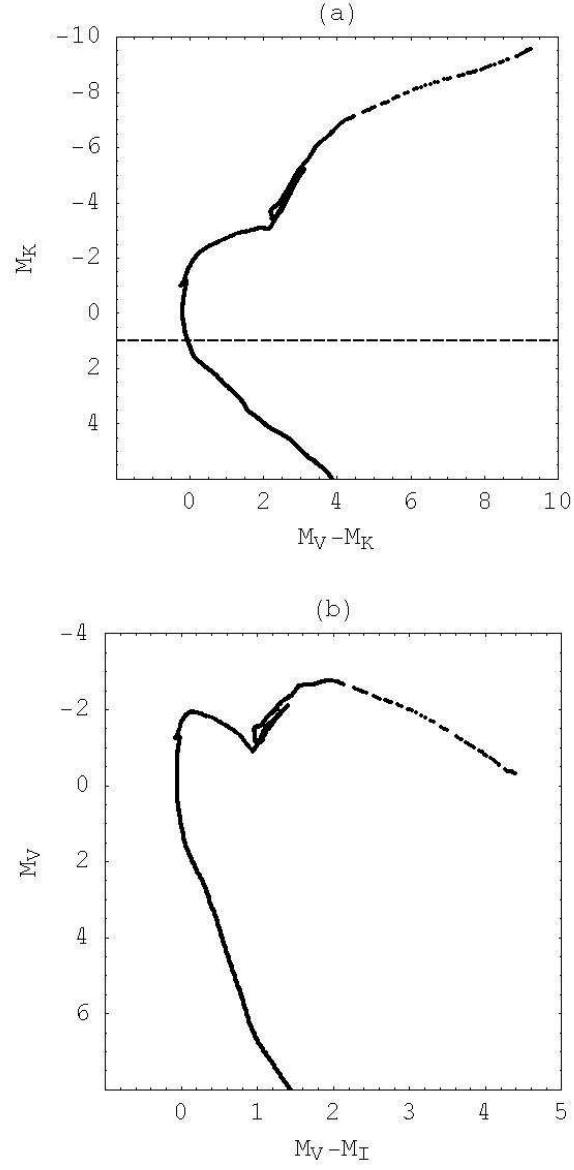


Fig. 1.— (a) $(M_K, M_V - M_K)$ color-magnitude diagram for P3; the dashed line represents the boundary between the two samples of stars re-combined with different weights in the luminosity function. (b) $(M_V, M_V - M_I)$ color-magnitude diagram for P3.

M_K	n_{P3}	$n_{P1+P2} \times 10^{-3}$	$n_{\text{Bulge}} \times 10^{-6}$	$n_{\text{Disk}} \times 10^{-6}$
-10.25	0	0	0	0.0054
-9.75	0.06	0	0	0.0054
-9.25	0.038	0	0	0.032
-8.75	0.04	0	0	0.07
-8.25	0.02	0	0	0.12
-7.75	0.024	0	0	0.12
-7.25	0.038	0.12	0.15	0.2
-6.75	0.07	0.54	0.68	0.98
-6.25	0.095	0.86	1.1	1.5
-5.75	0.097	0.9	1.1	1.5
-5.25	0.49	1.1	1.4	2.
-4.75	1.1	1.6	2.	2.9
-4.25	1.3	2.1	2.6	4.2
-3.75	11	3.5	4.4	6.8
-3.25	3.6	5.5	6.9	12
-2.75	0.091	5.2	6.5	12
-2.25	0.17	7.9	9.8	26
-1.75	0.18	34	42	124
-1.25	7.4	42	53	35
-0.75	17	26	33	38
-0.25	29	24	30	47
0.25	49	33	41	81
0.75	90	48	60	152
1.25	127	67	83	297
1.75	237	121	151	527
2.25	254	349	436	910
2.75	300	677	846	1550
3.25	309	1317	1645	2249
3.75	443	2272	2839	3375
4.25	555	3505	4380	4613
4.75	511	4027	5032	4436
5.25	752	4600	5748	6587
5.75	899	6754	8440	8272

Table 1: Binned luminosity functions in the K -band for P3, P1+P2, the bulge and the disk of M31. As each bin spans 0.5 magnitudes, the number of stars in each bin is just the tabulated value of n_{P_j} multiplied by 0.5.

M_V	n_{P3}	$n_{P1+P2} \times 10^{-3}$	$n_{Bulge} \times 10^{-6}$	$n_{Disk} \times 10^{-6}$
-8.25	0	0	0	0.0054
-7.75	0	0	0	0
-7.25	0	0	0	0.027
-6.75	0	0	0	0.0054
-6.25	0	0	0	0.0054
-5.75	0	0	0	0
-5.25	0	0	0	0.022
-4.75	0	0	0	0.038
-4.25	0	0	0	0.054
-3.75	0	0	0	0.12
-3.25	0	0	0	0.25
-2.75	0.22	0.0052	0.0065	0.37
-2.25	0.74	0.062	0.078	0.84
-1.75	7.	0.32	0.4	1.7
-1.25	21	0.96	1.2	4.1
-0.75	22	2.5	3.1	12
-0.25	35	6.5	8.1	30
0.25	53	9.7	12	57
0.75	80	51	63	165
1.25	98	31	38	97
1.75	118	26	33	148
2.25	138	33	41	213
2.75	132	41	51	329
3.25	150	64	80	551
3.75	166	235	294	928
4.25	178	826	1033	1382
4.75	205	1021	1276	1542
5.25	223	1317	1646	1748
5.75	233	1512	1890	1932
6.25	247	1706	2131	2046
6.75	248	1754	2192	2073
7.25	258	1897	2370	2227
7.75	299	2253	2815	2609

Table 2: Binned luminosity functions in the V -band for P3, P1+P2, the bulge and the disk of M31.

2.2. P1+P2

On a scale a bit larger than P3, the supermassive black hole in M31 is surrounded by two larger clusters, called P1 and P2. Actually, P1 and P2 are parts of the same eccentric disk orbiting the central black hole, with P2 being composed of stars at the periapsis and P1 by stars at the apoapsis (Tremaine 1995; Peiris & Tremaine 2003).

The spatial distribution of the whole system was obtained by Peiris & Tremaine (2003) fitting the brightness profile of a simulated sample of 10^7 stars with orbital parameters randomly chosen from some suitable distributions. We have followed their steps, simulating the same number of stars using the best fit parameters of their non-aligned model, which provides an excellent fit to the observed brightness profile of P1+P2. In Figure 2a we show the brightness profile thus obtained. For all the details relative to the eccentric disk model, the reader is referred to Peiris & Tremaine (2003). To give an idea of the shape of the cluster P1+P2, we just mention that the scale of its extension is fixed by the parameter $a_0 = 1.37$ pc, its inclination along the line of sight is $\theta_i = 54.1^\circ$, its thickness is roughly controlled by the combination $a_0\sigma_I^0$, with $\sigma_I^0 = 24.6^\circ$. For every star, the eccentricity is a function of the semiaxis of the orbit with several parameters. It is roughly peaked at $e = 0.5$.

Binning our simulated distribution of stars, we then easily obtain the spatial distribution function $f_{P1+P2}(x, y, z)$, to be used in the lensing calculations.

In the kinematic calculations, since the stars behind the black hole are closer to P2, we have used the average rotation velocity of P2, estimated as $v_{P2} = 220 \text{ km s}^{-1}$ with dispersion $\sigma_{P2} = 100 \text{ km s}^{-1}$ (Peiris & Tremaine 2003).

The characteristics of the stars composing P2 and P1 are quite similar to those of typical bulge stars. We have therefore used the bulge sample illustrated in § 2.3. Here we just mention that we have normalized this sample in the V -band, using $V_{P1+P2} = 12.55 \text{ mag}$ (Peiris & Tremaine 2003). With this normalization, we have built the luminosity functions in the K -band and in the V -band, as shown in Table 1. Some considerations on these functions are included in the following section.

2.3. Bulge

The bulge of M31 has been studied in great detail by Kent (1989), who traced precise luminosity and density contours. By interpolating these contours, it is possible to build a very accurate spatial distribution. We shall refer to this distribution as f_{Bulge} . The inclination of the plane of symmetry of the bulge is $i_{\text{Bulge}} = 77^\circ$. The bulge is assumed to have negligible

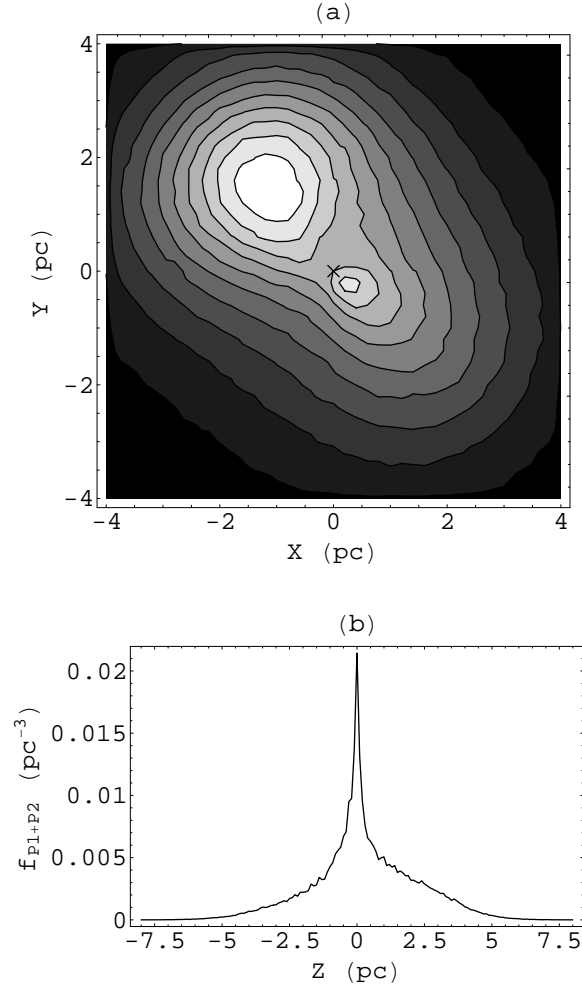


Fig. 2.— (a) Reconstructed brightness profile of the central cluster P1+P2, obtained following the prescriptions of Peiris & Tremaine (2003); north is up and east is left; the cross indicates the position of the central black hole. P1 is the brighter cluster, whereas P2 is the smaller one appearing closer to the black hole. (b) Spatial distribution of the cluster P1+P2 along the line connecting the observer with the black hole. The positive Z -axis points toward the observer.

rotation and constant dispersion velocity $\sigma_{\text{Bulge}} = 160 \text{ km s}^{-1}$.

In order to generate viable luminosity functions for the bulge, we have used the program IAC-STAR by Aparicio & Gallart (2004) in this case as well. In particular, following Sarajedini & Jablonka (2005), we have supposed that the bulge (and also P1+P2) were generated by a single starburst occurred 12.6 Gyr ago with metallicity following a closed box law

$$\frac{dN}{dZ} = \frac{1}{y} e^{(Z-Z_0)/y}, \quad (4)$$

with $Z_0 = 0$ and yield y equal to the solar metallicity $Z_{\odot} = 0.019$. With these specifications, we have generated 10^5 stars with $M_K < 6$ and 10^5 stars with $M_K < 1$. Before combining the two samples, we have randomly removed stars at the lower end of the metallicity distribution ($Z < 0.004$), in order to reproduce the data of Sarajedini & Jablonka (2005) as accurately as possible. This additional cut has reduced the two samples by roughly 10%. Figure 3 shows two color-magnitude diagrams of the combined sample of bulge stars. By comparing with the real ones studied by Sarajedini & Jablonka (2005), it is possible to appreciate the accuracy of our sample.

The luminosity profile introduced by Kent (1989) is obtained in the r -band of the Thuan and Gunn filter set. Assuming $r - K = 2.9$ (Olsen et al. 2006), we can directly normalize the luminosity function in the K -band and consequently in the V -band. The final results are included in Tables 1 and 2.

The bulge RGB lies in the range $-1 > M_K > -7.5$. The TOP is at $M_K \simeq -3$ rather than $M_K = 0$ as in P3. The red clump is peaked at $M_K = -1.25$ and is also evident in the V -band at $M_V = 0.75$.

2.4. Disk

The disk spatial distribution is modelled by

$$f_{\text{Disk}}(x, y, z) = \frac{1}{4\pi r_{\text{Disk}}^2 z_{\text{Disk}}} \exp \left[-\frac{\sqrt{x^2 + y^2}}{r_{\text{Disk}}} \right] \text{sech}^2 \left[\frac{z}{z_{\text{Disk}}} \right], \quad (5)$$

with disk scale $r_{\text{Disk}} = 5.5 \text{ kpc}$, thickness $z_{\text{Disk}} = 0.3 \text{ kpc}$ and inclination $i_{\text{Disk}} = 77^\circ$ (Widrow & Dubinski 2005).

The rotation velocity of the stars in the disk is $v_{\text{Disk}} = 250 \text{ km s}^{-1}$ with a negligible dispersion (Kent 1989).

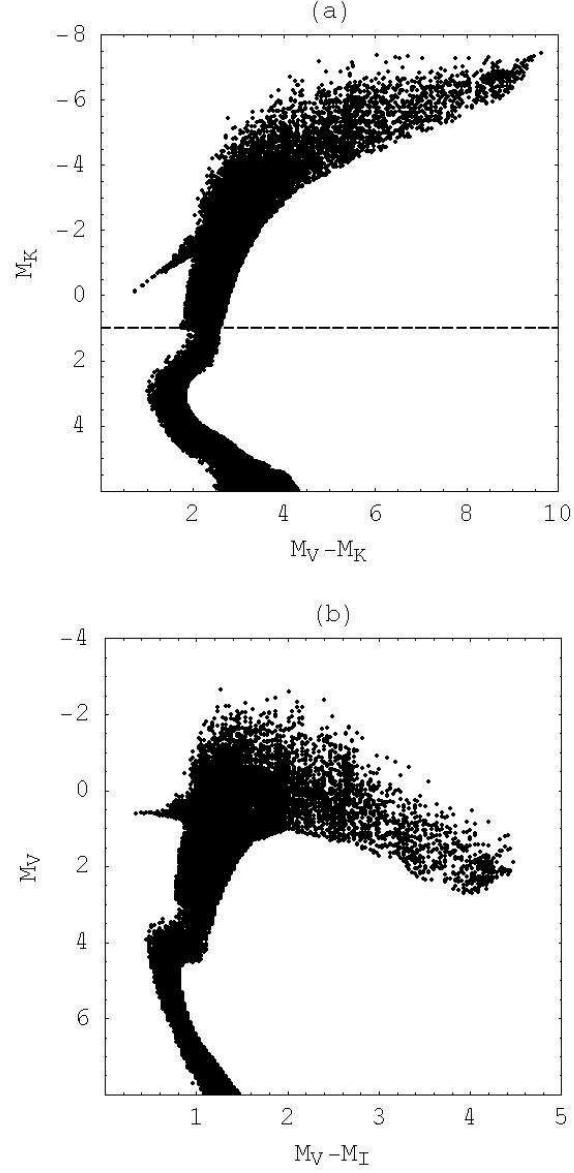


Fig. 3.— (a) $(M_K, M_V - M_K)$ color-magnitude diagram for the bulge and the cluster P1+P2; the dashed line represents the boundary between the two samples of stars re-combined with different weights in the luminosity function. (b) $(M_V, M_V - M_I)$ color-magnitude diagram for the bulge and P1+P2.

The disk star formation history is quite different from the one followed by the bulge and presumably by the central cluster stars. Following Hodge (1989), Williams (2002) and Bellazzini et al. (2003), we take a simple Population I model with a constant star formation rate throughout the history of M31 and constant solar metallicity. With these assumptions, we have run the program IAC-STAR obtaining 10^5 stars with $M_K < 6$ and more 10^5 stars with $M_K < 1$. The color-magnitude diagrams so-obtained are shown in Figure 4.

The normalization of our sample of stars has been determined comparing the total luminosity in the R -band to the total luminosity as indicated by Widrow & Dubinski (2005) $R_{\text{Disk}} = -21.4$. Finally, the correctly normalized luminosity function in the K -band and in the V -band have been included in Tables 1 and 2.

With respect to the other populations, the disk has a complete main sequence extending up to $M_K \simeq -7$ and $M_V \simeq -7$. Moreover, there are also some Red Supergiants (RSG) at $M_K = -10$ and $M_V = -8$. The existence of these supergiants mainly affects the V -band luminosity function, since it makes the disk luminosity function start at much brighter magnitudes with respect to the other populations. The red clump is peaked at $M_K = -1.75$ and $M_V = 0.75$, though almost contiguous to the MS in the V -band.

3. Basics of gravitational lensing

In this section we shall briefly recall some definitions used in standard gravitational lensing. This will prepare the ground for the analysis to be presented in the following sections.

The supermassive black hole in the center of M31 can be modelled as a simple point lens, with mass $M = 1.4 \times 10^8 M_\odot$, placed at a distance $D_{\text{OL}} = 760$ kpc from the Sun (Bender et al. 2005). We define the optical axis as the line joining the observer to the lens. For a source behind the black hole at distance D_{LS} from it, the lens equation takes the form

$$\beta = \theta - \frac{\theta_E^2}{\theta}, \quad (6)$$

where β is the angle between the line joining the observer to the source and the optical axis, θ is the angle formed by the observed image with the optical axis and

$$\theta_E = \sqrt{\frac{4GM}{c^2} \frac{D_{\text{LS}}}{D_{\text{OL}} D_{\text{OS}}}} \quad (7)$$

is the Einstein angle and $D_{\text{OS}} = D_{\text{OL}} + D_{\text{LS}}$ is the distance from the observer to the source. As the source distances considered in this paper are at most of the order of a few kpc behind the lens, we generally have $D_{\text{OS}} \simeq D_{\text{OL}}$.

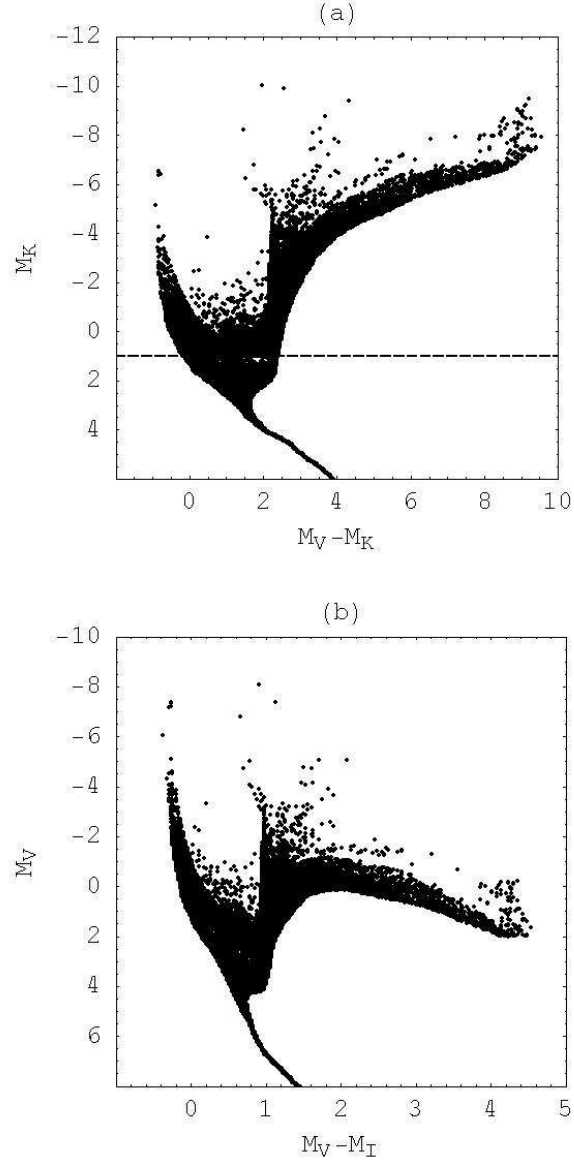


Fig. 4.— (a) $(M_K, M_V - M_K)$ color-magnitude diagram for the disk; the dashed line represents the boundary between the two samples of stars re-combined with different weights in the luminosity function. (b) $(M_V, M_V - M_I)$ color-magnitude diagram for the disk.

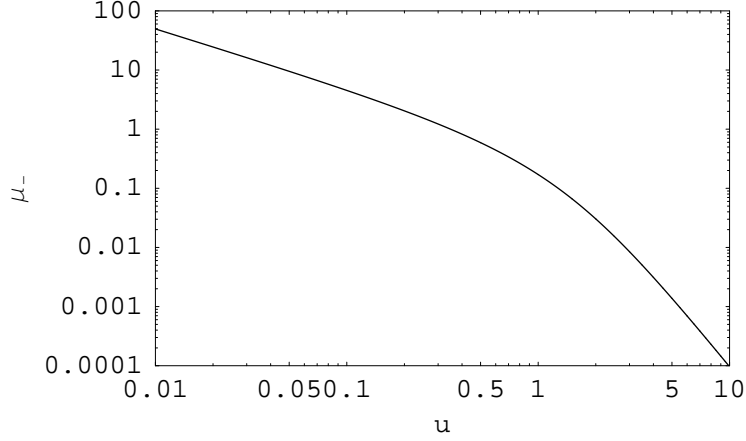


Fig. 5.— Magnification of the secondary image as a function of the source position normalized to the Einstein angle.

Solving the lens equation for θ , we obtain the position of the two images

$$\theta_{\pm} = \frac{1}{2} \left(\beta \pm \sqrt{\beta^2 + 4\theta_E^2} \right). \quad (8)$$

These two images are magnified by a factor

$$\mu_{\pm} = \frac{u^2 + 2}{2u\sqrt{u^2 + 4}} \pm \frac{1}{2}, \quad (9)$$

where $u = \beta/\theta_E$ is the source angular position normalized to the Einstein angle.

Figure 5 shows the magnification of the secondary image as a function of the normalized source position. It clearly shows how the dependence of the magnification on u changes from u^{-1} to u^{-4} as we go from the regime of good alignment ($u \ll 1$) to the regime of bad alignment ($u \gg 1$), the Einstein angle representing the scale of the transition between the two regimes.

When the source is far from the optical axis ($\beta \gg \theta_E$) the secondary image has very low magnification and becomes unobservable. Our aim is to determine the probability of seeing the secondary images of sources in M31, which will typically become observable when β is of the same order of magnitude as θ_E . We then note that the angular separation of the secondary image from the central black hole is always of the order of the Einstein angle for $\beta \lesssim \theta_E$. The order of magnitude of the Einstein angle in the physical situation we are

considering is

$$\theta_E = 44 \text{ mas} \left(\frac{D_{LS}}{\text{kpc}} \right)^{1/2}. \quad (10)$$

The Einstein angle is of order $0.1''$ for sources as far as a few kpc, whereas it drops to a few mas when the source is closer than 100 pc. We can thus conclude that in order to observe the secondary images of sources closer than 1 kpc to the central black hole we need very high angular resolution, only achievable by interferometric techniques, such as those employed in the VLTI, Keck and LBT. This gives an advantage to source populations distributed on a larger scale (bulge and disk) with respect to the central clusters P1+P2 and P3. However, distinguishing a secondary image at $0.1''$ from the central black hole from other sources is by no means easy and certainly demands high resolution as well.

Since we are speaking about lensing by a supermassive black hole, it is interesting to check that the weak deflection paradigm holds for all the interesting events. Higher order images formed by photons performing loops around the central black hole show up very close to the black hole shadow border, which has a radius of $\theta_{sh} = 9 \mu\text{as}$ (Darwin 1959; Virbhadra & Ellis 2000; Bozza 2002). In order to detect such images, a much greater effort with respect to ordinary lensing images would be necessary. For this reason, we will not consider them in the present analysis.

It remains to check whether the secondary image can always be correctly described in the weak deflection limit. This can be verified by comparing the position of the image θ_- with the radius of the shadow border θ_{sh} . Approximating θ_- by θ_E , the ratio θ_{sh}/θ_E gives an estimate of the error we commit by neglecting the next to leading order term in the deflection angle (Keeton & Petters 2005). It is easy to calculate that the error is 2% at $D_{LS} = 0.1$ pc and 6% at $D_{LS} = 0.01$ pc. As it will be evident in § 6, where we calculate the distribution of the events as a function of the source distance, only the low D_{LS} tail of the P3 distribution is affected by these errors and then only marginally. Considering the low relevance of this tail in the total estimates and the uncertainties in the P3-population modelling, we will simply ignore any strong deflection effect in our analysis.

4. Number of lensed sources

This section contains the main calculation of this work, namely the number of expected lensing events at a given time for each source population around the supermassive black hole in M31. We first introduce the methodology that we have followed and then present our estimates for each population at the end of the section. We will focus on the K -band, with

analogous considerations holding for the V -band.

Consider a source of absolute magnitude M_K . The observed magnitude K is

$$K = M_K + 5 \log_{10} \frac{D_{\text{OS}}}{10 \text{ pc}} + A_K, \quad (11)$$

where $A_K = 0.1$ is the extinction in the K -band (Olsen et al. 2006). If the source suffers gravitational lensing, its secondary image has apparent magnitude

$$K_- = K - 2.5 \log_{10} \mu_-, \quad (12)$$

with μ_- given by equation (9).

If we fix a threshold magnitude K_{thr} for the detection of the secondary image, only the sources sufficiently magnified will have a secondary image with $K_- < K_{\text{thr}}$. The minimum magnification needed to bring a source with absolute magnitude M_K above threshold can be found by simply inverting equation (12) with $K_- = K_{\text{thr}}$

$$\mu_- = 10^{-0.4(\Delta K - 24.5)}, \quad (13)$$

where $\Delta K = K_{\text{thr}} - M_K$.

As the magnification is a function of the normalized source position angle u through equation (9), there exists a limiting value for u (which we shall indicate by u_Z) such that a source with absolute magnitude M_K has a secondary image just at the threshold value K_{thr} . This can be found inverting equation (9)

$$u_Z(\mu_-) = \left[2\mu_-(1 + \mu_-) + (1 + 2\mu_-)\sqrt{\mu_-(1 + \mu_-)} \right]^{-1/2}. \quad (14)$$

Defining $\beta_Z = \theta_E u_Z$, all sources with $\beta < \beta_Z$ have a secondary image brighter than K_{thr} . Finally, we can also define the radius of the lensing zone at distance D_{LS} , as the radius of the circle containing the sources with magnitude M_K whose secondary image is magnified above K_{thr} . Of course, the radius of this circle is simply $R_Z = \beta_Z D_{\text{OS}}$. For any value of the distance D_{LS} , only sources with $r < R_Z$ have an observable secondary image. As D_{LS} varies, we can thus define a lensing zone with radius $R_Z(D_{\text{LS}})$ centered on the optical axis and that contains all the sources with absolute magnitude M_K that give rise to observable gravitational lensing effects. More explicitly, the radius of the lensing zone is

$$R_Z = 0.16 \text{ pc} \left(\frac{D_{\text{LS}}}{\text{kpc}} \right)^{1/2} u_Z(\mu_-(\Delta K)), \quad (15)$$

which clearly shows that the radius of the lensing zone grows with the square root of the distance of the source from the black hole. The dependence on the absolute magnitude of

the source and the threshold fixed by observations is stored in the function $u_Z(\mu_-(\Delta K))$. The brighter the source and the fainter the threshold, the larger the lensing zone.

The probability of finding a single star of absolute magnitude M_K in the lensing zone defined by the threshold magnitude K_{thr} is obtained integrating the spatial distribution of the population to which the source belongs in the domain contained within the lensing zone

$$\Pi_{P_j}(M_K, K_{\text{thr}}) = \int_0^\infty dD_{\text{LS}} \int_0^{R_Z} dr \, r \int_0^{2\pi} d\phi f_{P_j}(D_{\text{LS}}, r, \phi), \quad (16)$$

where we recall that R_Z is a function of D_{LS} , M_K , and K_{thr} . In the evaluation of the spatial distribution one must take care of the correct geometric orientation in the space of the population considered, as specified in § 2.

Finally, the total number of lensed sources with a secondary above threshold is

$$N_{P_j}(K_{\text{thr}}) = \int n_{P_j}(M_K) \Pi_{P_j}(M_K, K_{\text{thr}}) dM_K. \quad (17)$$

Figure 6a shows the estimated number of lensing events for each of the four source populations considered in this paper as a function of the threshold magnitude K_{thr} . Repeating the same steps, we can get a similar plot for observations lead in the V -band, with a threshold magnitude V_{thr} as shown in Figure 6b.

We see that P3 gives a practically negligible contribution. The stars in P3 are too few and too close to the supermassive black hole. The lensing zone is indeed too restricted at distances of the order of a pc to get a sizeable number of events.

The situation for P1+P2 is much better, because this cluster extends to larger radii and is more populated. However, we have to push the threshold magnitude to $K_{\text{thr}} = 27$ or $V_{\text{thr}} = 30$ in order to have at least one expected event. The estimated number of events for the disk is very similar to that of P1+P2.

The bulge is by far the best reservoir of good sources for gravitational lensing by the central black hole. The number of expected events is already larger than one at $K_{\text{thr}} = 24$ or $V_{\text{thr}} = 27$, reaching more than one hundred at $K_{\text{thr}} = 30$ or $V_{\text{thr}} = 32$. Comparing the plots in the K -band and the V -band, we can note that redder populations such as P1+P2 and the bulge are slightly depressed when going from the K -band to the V -band. The disk supergiants, not present in other populations, keep the the disk number of events higher at low values of V_{thr} with respect to the other populations.

Roughly, the plot in the V -band is very similar to the plot in the K -band, but is shifted to higher values of V_{thr} by 2.5 magnitudes. This apparent gap between the two bands is

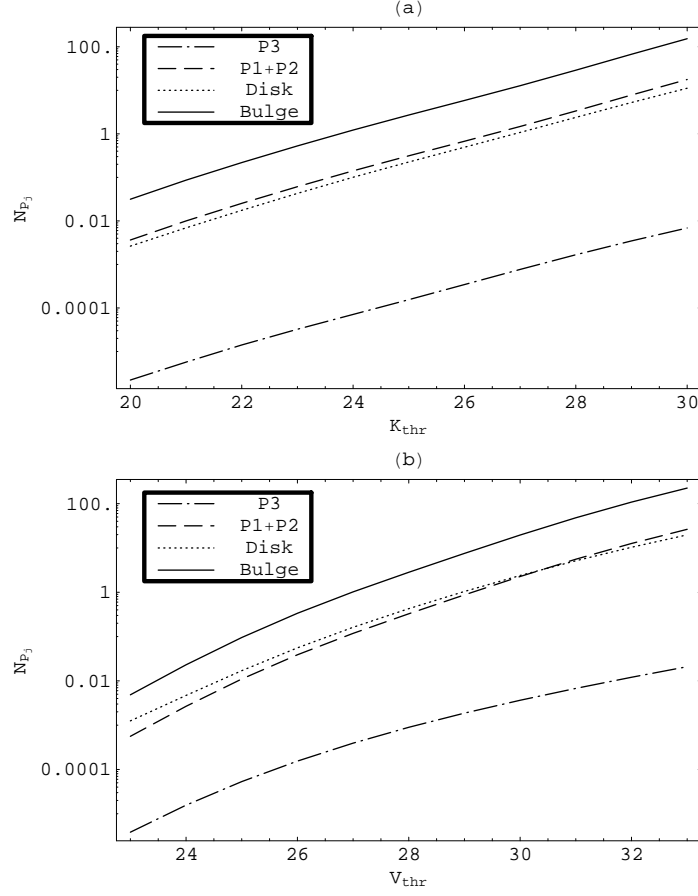


Fig. 6.— (a) Number of expected lensing events as a function of the threshold magnitude for the secondary image in the K -band. (b) Number of expected lensing events as a function of the threshold magnitude for the secondary image in the V -band. Note the different range in the ordinate axis in the two plots.

actually completely recovered when one compares the signal to noise ratio (SNR) in the two bands. In fact, a source with $V - K = 0$ emits 5.77 photons in the V -band for each photon in the K -band (Cox 2001). In the background-limited regime, the expected noise due to the 4 populations considered in this paper can be easily estimated thanks to the spatial distributions and luminosity functions introduced in § 2. Indeed we find that for images with the same FWHM the SNR in the V -band is 2.5 magnitudes better than in the K -band. This justifies our choice to plot our expectations in the intervals $20 < K_{\text{thr}} < 30$ and $23 < V_{\text{thr}} < 33$. Furthermore, if the diffraction limit in the two bands is reached with the same aperture, one gets an additional bonus of 1.5 magnitudes for the V -band. However, at the present time, the largest interferometers such as VLTI, Keck and LBT are not designed for observations in the V -band and therefore only the K -band can take advantage of the resolutions available at such long-baseline facilities.

The expectations plotted in Figure 6 are also summarized in Tables 3 and 4. Recall that these estimates give the number of secondary images above threshold simultaneously present at a given time. See § 8 and § 9 for a discussion on their evolution in time. It should be noted that the estimates presented in this section do not take into account the angular separation of the secondary images from the central black hole. § 7 is devoted to that issue.

5. Magnitude of the lensed sources

The number of expected events as calculated in the previous section is obtained by integrating over the whole range of possible magnitudes for the sources. It is interesting to evaluate the contributions of sources with different magnitudes to the final result. In Figure 7 we show the integrand of equation (17) for all four populations as a function of the source magnitude M_K and the threshold magnitude K_{thr} . For each value of K_{thr} the function dN_{P_j}/dM_K has been normalized to unity. Figure 8 shows the same distributions in the V -band.

Schematically, we can say that low luminosity stars are more numerous, whereas brighter stars enjoy a larger lensing zone and consequently a larger lensing probability. The surfaces in Figures 7 and 8 are the outcome of the interplay of these two opposite tensions. At lower thresholds, the distributions are peaked on the most luminous stars. As we increase the threshold, less luminous populations become predominant.

As regards the K -band, in the distributions shown in Figure 7 we can clearly identify the tip of the RGB in the high luminosity peak dominating at lower values of the threshold. At intermediate values of K_{thr} , the red clump gives the highest contribution. At fainter

K_{thr}	N_{Bulge}	N_{Disk}	$N_{\text{P1+P2}}$
20	0.032	0.0026	0.0036
21	0.086	0.0069	0.01
22	0.22	0.017	0.025
23	0.53	0.043	0.061
24	1.2	0.1	0.14
25	2.7	0.23	0.31
26	5.8	0.49	0.68
27	13	1.1	1.5
28	29	2.4	3.4
29	67	5.3	7.8
30	153	11	18

Table 3: Expected number of events for sources in the bulge, the disk and P1+P2 for different threshold magnitudes in the K -band for the secondary image.

V_{thr}	N_{Bulge}	N_{Disk}	$N_{\text{P1+P2}}$
23	0.0048	0.0013	0.00056
24	0.023	0.0047	0.0027
25	0.095	0.017	0.011
26	0.34	0.056	0.039
27	1.	0.16	0.12
28	2.8	0.43	0.33
29	7.5	1.	0.87
30	20	2.4	2.3
31	48	5.1	5.6
32	108	10	13
33	225	20	26

Table 4: Expected number of events for sources in the bulge, the disk and P1+P2 for different threshold magnitudes in the V -band for the secondary image.

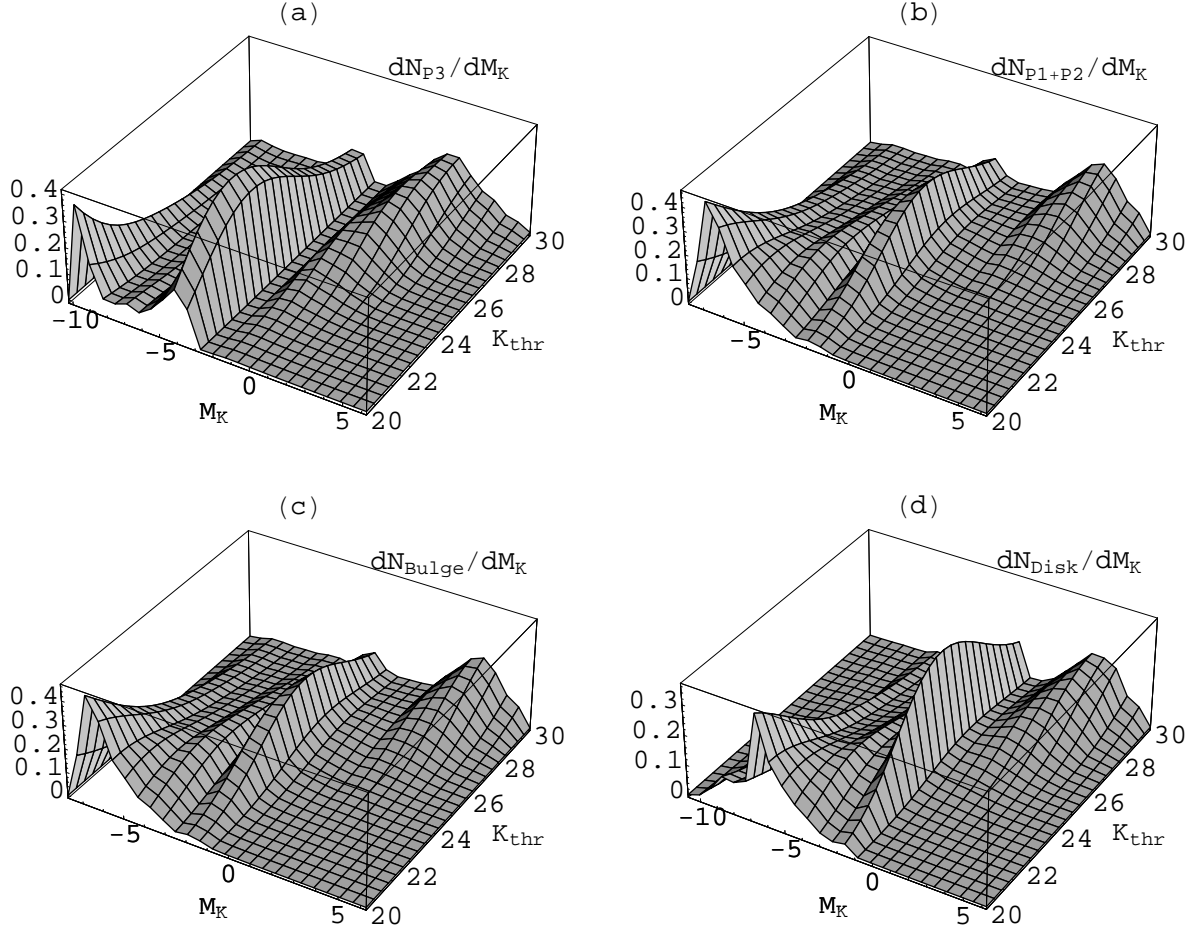


Fig. 7.— Relative contribution of sources with different absolute magnitudes to the total number of expected events for threshold magnitudes ranging from 20 to 30 in the K -band. (a) P3; (b) P1+P2; (c) bulge; (d) disk.

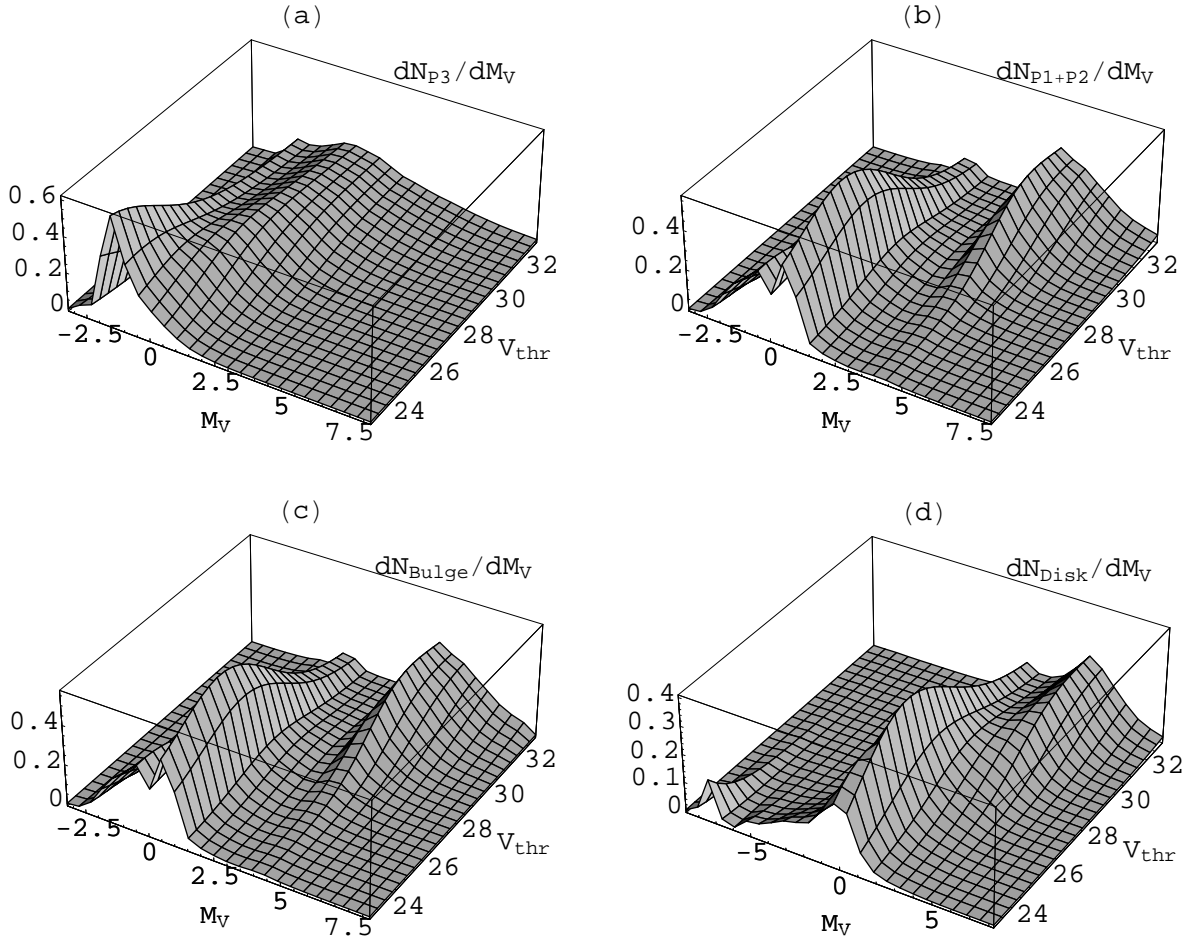


Fig. 8.— The same as Figure 7 in the V-band.

thresholds, the stars at the TOP become significant and finally overtake the red clump. It is interesting to note that the TOP peak gradually shifts to dimmer values of M_K as K_{thr} is increased and less luminous stars of the main sequence come into play. In the disk distribution, the brighter main sequence stars and the RSG also contribute to the first peak at low threshold values.

In the V -band, the difference between the four populations is made more manifest. We can note that P1+P2 and the bulge are characterized by just two peaks: the one at higher luminosities is due to the red clump at $M_V \simeq 0$ and the dimmer at $M_V \simeq 4$ is made up of stars at the TOP. The RGB is almost horizontal and therefore there is no other peak at lower values of M_V . In P3 the red clump and the TOP give rise to two consecutive peaks at $M_V \simeq -1.5$ and $M_V \simeq 0$ respectively. As the threshold is increased, the distribution flattens because of the contribution of progressively fainter stars coming into play. The disk distributions start with the peak at $M_V \simeq -8$ due to the RSG, which are absent in the other populations. These stars give rise to the different behavior of the disk at low thresholds, already discussed in the previous section. At intermediate thresholds the red clump becomes dominant and is later followed by the TOP contribution, which first forms a shoulder to the red clump peak and then becomes dominant.

Another important point can be anticipated noting that the distributions for P1+P2 and the bulge are always practically identical. This proves that differences in the spatial distribution have very little influence in selecting the class of sources (luminous or dim) for gravitational lensing. This point will be better explained in the next section, where we show that the magnitude and distance distributions can be factorized in a first approximation.

As a final consideration, we see that the contribution of stars at $M_K \simeq 6$ or $M_V \simeq 8$ is always negligible for the thresholds considered in this paper. This provides an *a posteriori* justification of the irrelevance of the faint end issue of the luminosity function in our calculations, as anticipated in § 2.

6. Distance of the lensed sources

The four source populations considered in this paper fill different regions of M31, at various distances from the center. It is interesting to calculate the distribution of the sources suffering gravitational lensing as a function of their distance from the central black hole D_{LS} . Actually, since the distributions are spread over several orders of magnitudes in distance, we prefer to present the distributions in $\log_{10} D_{\text{LS}}$. In order to get this distribution for each population, we return to equations (16) and (17) and reverse the order of integration in D_{LS}

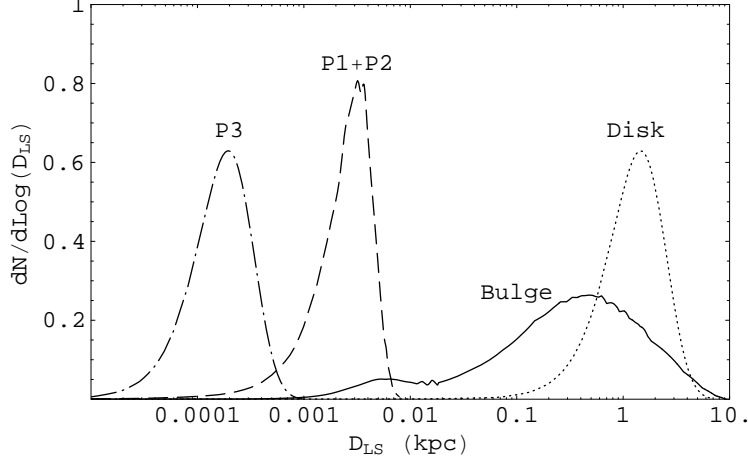


Fig. 9.— Distributions for the distance of the lensed sources from the black hole.

and M_K

$$\frac{dN_{P_j}}{d \log_{10} D_{LS}} \propto D_{LS} \int dM_K n_{P_j}(M_K) \int_0^{R_Z} dr r \int_0^{2\pi} d\phi f_{P_j}(D_{LS}, r, \phi). \quad (18)$$

The distributions so-obtained are shown in Figure 9, after having been normalized to unity. The plots are obtained for $K_{\text{thr}} = 24$, but the distributions for different thresholds and even for different bands are practically indistinguishable. This is a consequence of the fact that the radius of the lensing zone R_Z is always much smaller than the scale of variation of all spatial distributions. Then it is possible to approximate the spatial distributions in the integrals (16) and (18) with the values they assume at the center of the disk of radius R_Z and replace the integral over r and ϕ by $\pi R_Z^2 f_{P_j}(D_{LS}, 0, 0)$. Since the dependence on D_{LS} in the radius of the lensing zone factors out, being always $\sqrt{D_{LS}}$, the spatial distribution and the magnitude distributions are effectively factorized. This decoupling is not possible when we consider the angular position and the velocity of the images, as will be shown in the succeeding sections.

The maximum lensing probability is reached by P3 at $D_{LS} = 0.19$ pc, by P1+P2 at $D_{LS} = 3.7$ pc, by the bulge at $D_{LS} = 0.48$ kpc and by the disk at $D_{LS} = 1.5$ kpc. With respect to the other populations, the distribution of the bulge events is less localized and presents a first subpeak at 5 pc. This is a consequence of the fact that although the bulge is sharply peaked at the center of the galaxy, it has a long tail decreasing at a lower rate with respect to the exponential tail characterizing the other distributions. Moreover, the other populations are more or less flattened on planes that never contain the line of sight, whereas

the bulge has a more spheroidal shape.

7. Position of the images

From the observational point of view, it is very important to determine the expected angular distance from the central black hole of the secondary images we are looking for. In practice, the choice of the facilities to employ in the search for these images is heavily influenced by the resolution required to resolve them. In this section, we derive the distribution of the secondary images generated by gravitational lensing with respect to their angular distance from the central black hole.

Suppose we want to calculate the fraction of sources belonging to a given population that generate a secondary image at an angular distance in the range $[\theta, \theta + d\theta]$. The angular position of these sources is determined through equation (6) as a function of θ and D_{LS} . We thus have to sum up the contributions of sources at different D_{LS} . Considering that $|\beta(\theta, D_{\text{LS}})|$ is a growing function of D_{LS} , the first contribution comes from a source at distance $D_{\text{min}}(\theta)$ such that $|\beta(\theta, D_{\text{min}})| = 0$. This distance can be explicitly calculated using equations (6) and (7). The last contribution comes from sources at the border of the lensing zone, whose distance $D_{\text{max}}(\theta)$ is such that $|\beta(\theta, D_{\text{max}})| = \beta_{\text{Z}}(M_K, K_{\text{thr}}, D_{\text{max}})$. This distance is also easily calculable (note that the absolute value is necessary because we are considering secondary images, i.e. images with $\theta < \theta_{\text{E}}$). Finally, for each source distance in the range $[D_{\text{min}}, D_{\text{max}}]$, we must sum up the contributions of all space elements lying on a circle of radius $D_{\text{OS}}|\beta(\theta, D_{\text{LS}})|$ centered on the optical axis at distance D_{LS} from the black hole.

As in the previous section, we prefer to calculate the distribution in $\log_{10} \theta$. Taking proper account of all the Jacobians, we have

$$\frac{dN_{P_j}}{d \log_{10} \theta} \propto \theta \int dM_K n_{P_j}(M_K) \int_{D_{\text{min}}}^{D_{\text{max}}} dD_{\text{LS}} D_{\text{OS}}^2 |\beta(\theta, D_{\text{LS}})| \left(2 + \frac{|\beta(\theta, D_{\text{LS}})|}{\theta} \right) \int_0^{2\pi} d\phi f_{P_j}(D_{\text{LS}}, \beta, \phi). \quad (19)$$

Equation (19) is for observations in the K -band. The distribution for observations in the V -band can be calculated similarly with the obvious replacements. Note that now it is impossible to factor the dependence on D_{LS} , K_{thr} and M_K as done in the previous section. As a consequence, the distribution of the angular positions of the images strongly depends on the threshold magnitude chosen.

In Figures 10 and 11 we show the distributions (normalized to unity at each threshold) for each source population and for values of the threshold magnitude ranging from 20 to 30 in

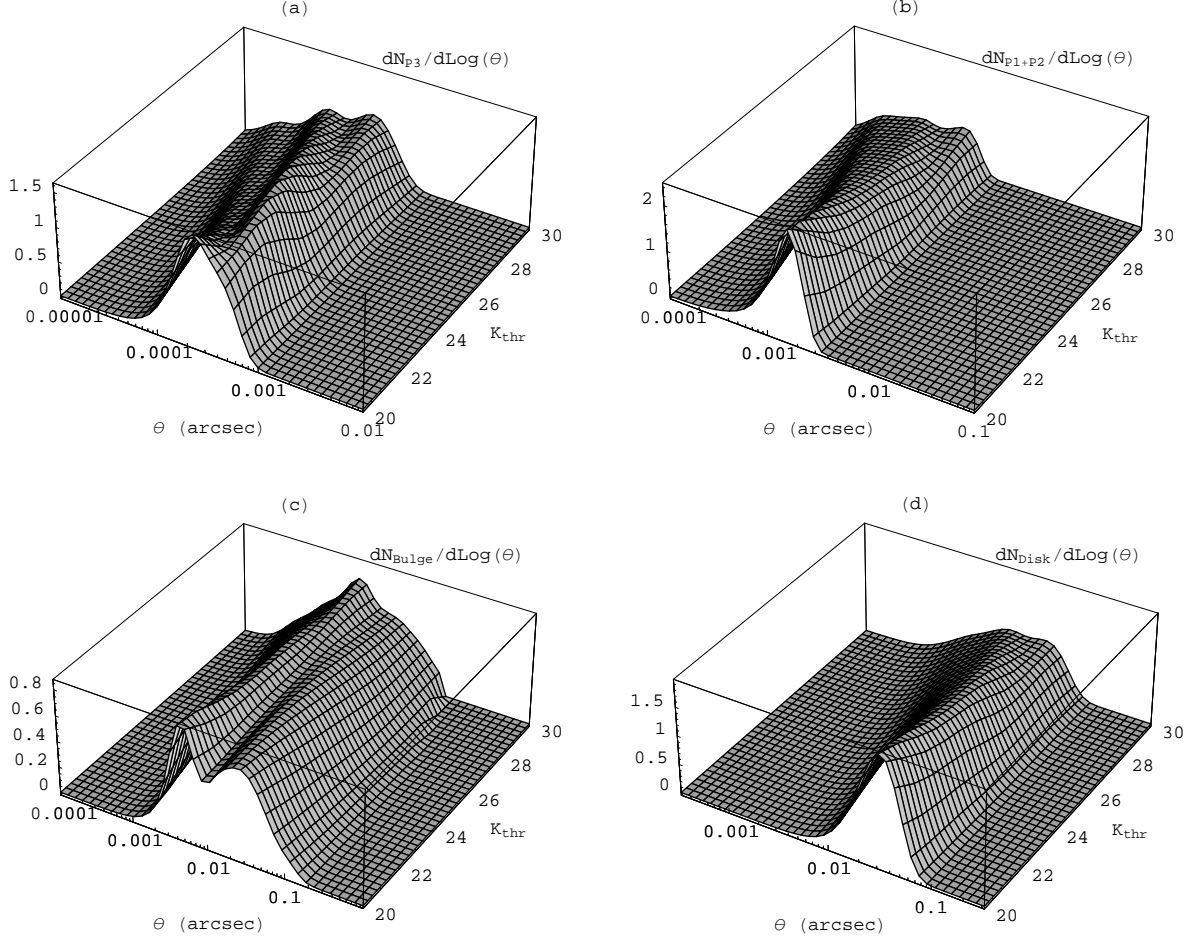


Fig. 10.— Distributions of the angular distances of the gravitational lensing secondary images from the black hole for the four source populations at different values of the threshold magnitude in the K -band. (a) P3; (b) P1+P2; (c) bulge; (d) disk.

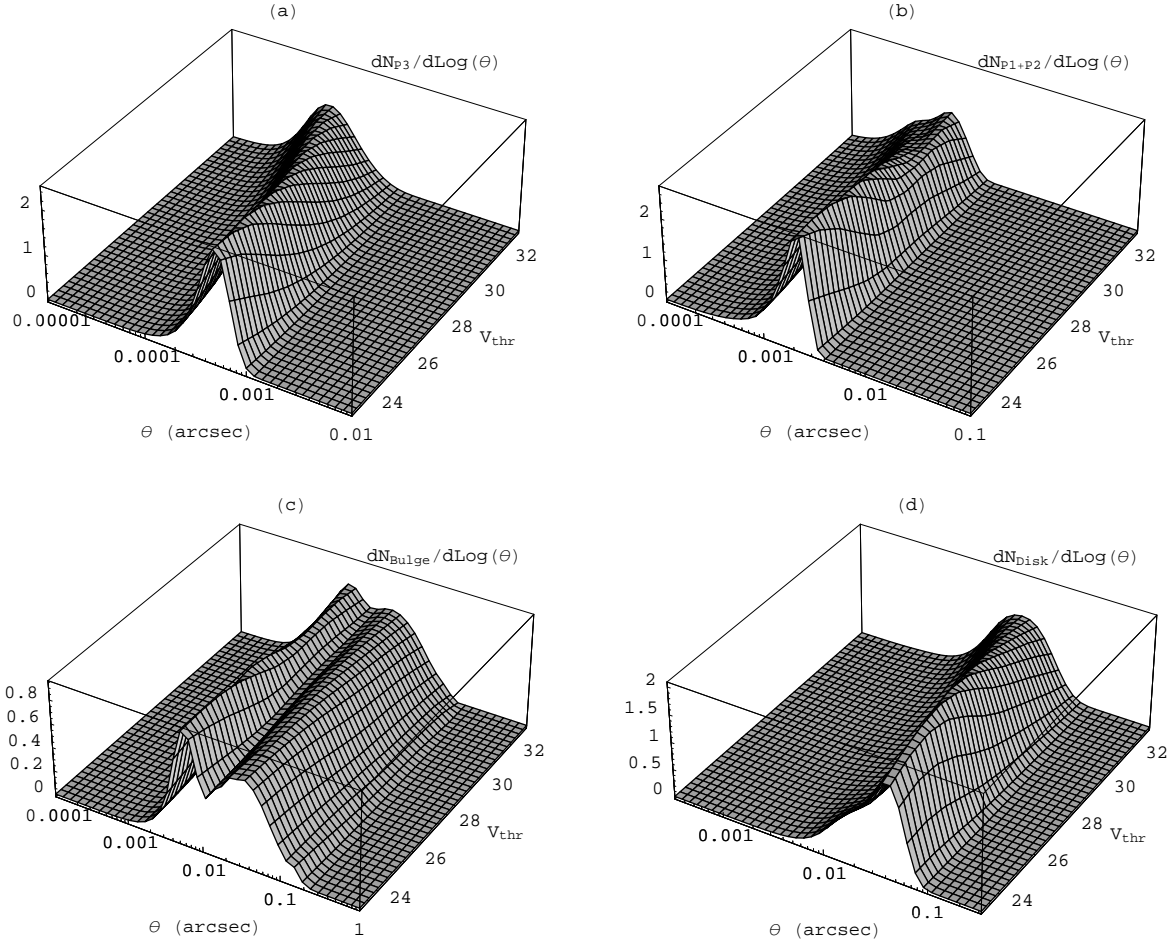


Fig. 11.— The same as Figure 10 in the V-band.

the K -band and from 23 to 33 in the V -band respectively. The images of sources belonging to P3 have angular distance in the range $[0.0001'', 0.001'']$, those belonging to P1+P2 appear at a few mas from the central black hole, those in the disk have angular distance in the range $[0.01'', 0.1'']$, whereas sources in the bulge can generate images with a larger spread of angular distances, from $0.001''$ to $0.1''$. In general, as we increase the threshold magnitude, the distributions move to slightly lower values of θ . This can be understood by the fact that lowering the threshold we accept fainter images generated by sources more distant from the optical axis, whose secondary images appear closer to the black hole. In practice, as a general rule, we learn that, in order to catch all fainter images one gets by performing deeper observations, one also needs better resolution. This shift is partly compensated by the existence of numerous intrinsically dim stars, which anyway need a very good alignment in order to generate a visible secondary image. These dim stars tend to keep the distribution at the highest possible value of θ , essentially fixed by the Einstein angle at the typical distance scale of the population.

Apart from this general behavior, we can clearly identify some of the populations discussed in § 5. For example, in the distribution for P3 in the K -band we can clearly distinguish three peaks at high threshold, corresponding to the tip of the RGB, the red clump and the TOP from left to right. These peaks are more smoothed in the distributions for P1+P2 and the disk. In the bulge, the double peak structure is mainly determined by its spatial distribution, which presents a long tail extending up to a few kpc. This long tail is responsible for the peak at $\theta \simeq 0.01''$. This can be seen by the fact that at $K_{\text{thr}} = 20$, at which we expect a single peak due to the tip of the RGB, we already have two evident peaks. Moreover, the same structure can be seen in the V -band distribution, notwithstanding the different magnitude distribution.

The V -band distributions appear to be less structured with just a very slight shift to lower values of θ with the increase of V_{thr} .

Summing up, we note that imaging the central regions of the nucleus of M31 with a resolution of the order of a few mas, as could be possible with the Keck or the LBT, will allow to catch secondary images of sources in the disk and a large part of those in the bulge, provided one reaches a faint enough K_{thr} (see discussion in § 10).

8. Velocity of the images

Up to now, we have just calculated the number of gravitational lensing events that are observable at a given time. It is very important to understand the timescale of the

variations of the geometric configuration of such lensing events. In fact, the strategies for the observations tightly depend on these timescales and can be very different for static or nearly static configurations as opposed to events with any secular development. As will be discussed in § 10, the detection of the motion of the images might be of key importance to identify genuine gravitational lensing events. This section is devoted to the presentation of the distributions of the expected velocities of the secondary images below a given threshold magnitude.

These distributions are obtained by a Montecarlo procedure. For each value of M_K and K_{thr} , we have generated 10^4 stars, randomly choosing their position within the lensing zone corresponding to these magnitudes. The velocities of these sources have been randomly extracted from a two-dimensional gaussian distribution centered on the rotation velocity v_{P_j} with dispersion σ_{P_j} . The values of these parameters are specified in § 2 for each population.

Once the sources have been generated, we have calculated the apparent proper motions of the corresponding secondary images by differentiating the standard formula for the position of the secondary image. The result is

$$v_\theta = \left| \frac{d\vec{\theta}_-}{dt} \right| = \frac{\sqrt{u^2 + 4 \sin^2 \phi}}{2} \left(\frac{1}{u} - \frac{1}{\sqrt{u^2 + 4}} \right) \frac{v}{D_{\text{Os}}}, \quad (20)$$

where v_θ is the modulus of the time derivative of the angular position of the secondary image, v is the modulus of the transverse velocity of the source and ϕ is the angle between the velocity and position vectors of the source.

The image velocity decreases as u^{-2} when the source is far away from the optical axis. In this limit, the secondary image is also very faint and close to the black hole. In the opposite limit, when $u \rightarrow 0$, the velocity diverges (except for the case $\phi = 0$). This is very well-known in microlensing studies, as the secondary image moves very rapidly when the source is at the closest approach distance.

With the velocities of the images thus calculated, we have constructed the distributions shown in Figures 12 and 13 for the K -band and V -band respectively. The proper motion has been expressed in milliarcseconds per year.

The expected apparent proper motions of the secondary images cover a very large range. All four populations generate images whose velocities generally lie between 0.01 and 0.1 mas/y, with very long tails extending one order of magnitude above and below these limits.

Going from lower to higher thresholds, all distributions significantly drift to lower values of the proper motion. This is clear from the fact that, at bright thresholds, very good

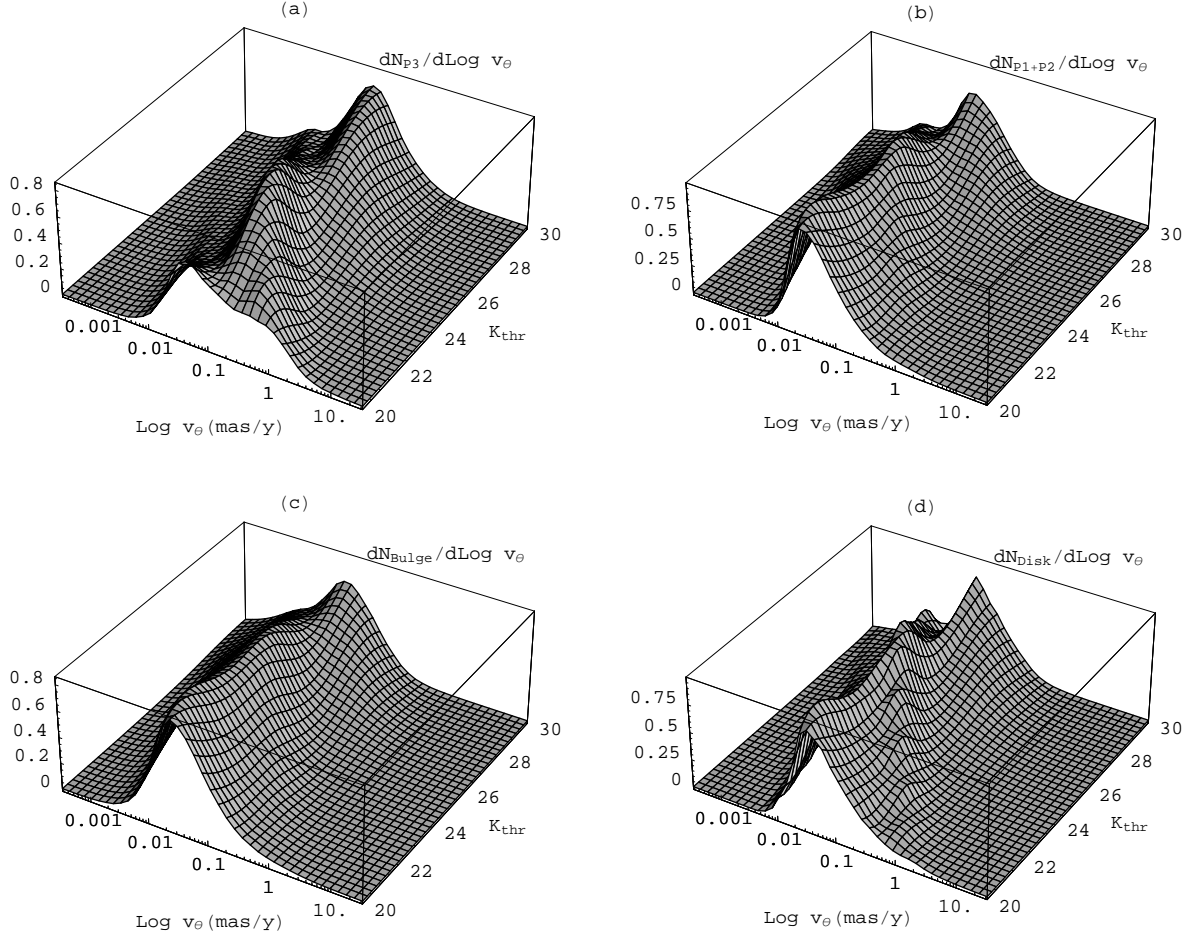


Fig. 12.— Distributions of the velocities of the gravitational lensing secondary images from the black hole for the four source populations at different values of the threshold magnitude in the K -band. (a) P3; (b) P1+P2; (c) bulge; (d) disk.

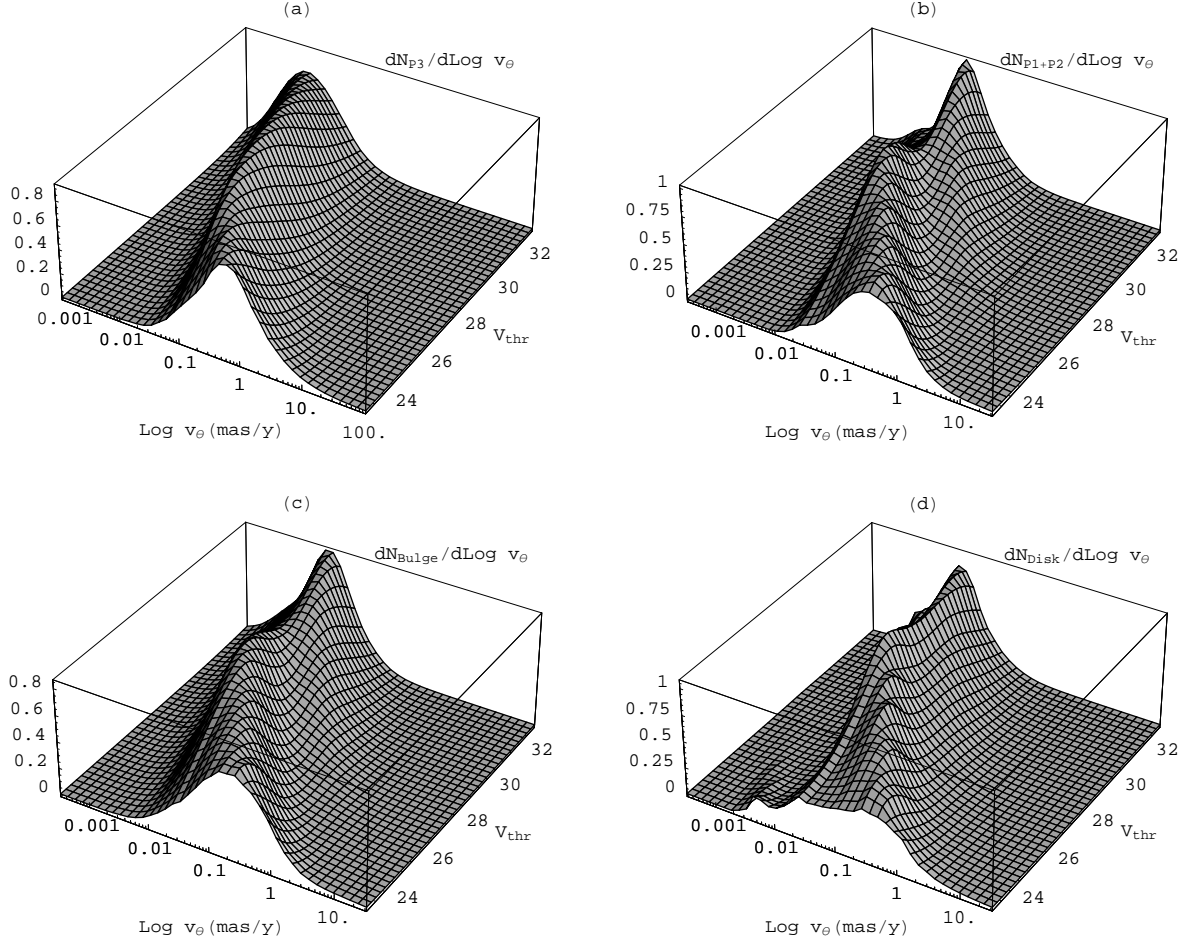


Fig. 13.— The same as Figure 12 in the V-band.

alignments generate higher velocities as it is evident from equation (20) and viceversa. Then, going to fainter thresholds, the lensing zone is enlarged, and less aligned sources participate in the distribution pulling it to lower values of v_θ . This is particularly evident in the V -band.

Thanks to the stronger dependence of the velocity distributions on the threshold magnitude, the internal structure of the four populations in terms of stellar components is made more evident. In the K -band we can clearly identify three peaks moving from right to left as K_{thr} is increased from 20 to 30. As usual, the peak on the left is due to the tip of the RGB, the central peak is due to the red clump and the one on the right is made up of TOP stars, coming into play at higher thresholds. In the V -band there is a first peak formed by red clump stars moving from high to low values of v_θ . At high thresholds the TOP stars are able to form a shoulder and then a second peak on the right of the red clump peak. At low values of V_{thr} the disk distribution is influenced by RSG, which form the tail at small v_θ . The contribution of RSG becomes subdominant already at intermediate thresholds, where it is taken over by red clump stars and finally by TOP stars.

9. Rate and duration of the events

An interesting quantity for the definition of the timescale of observational campaigns is the rate of the events, defined as the number of new detectable events occurring per unit time. It can be calculated by

$$\Gamma_{P_j} = \int dM_K n_{P_j} \int_0^\infty dD_{\text{LS}} 2 \int_0^{R_Z} dr \frac{1}{2\pi} \int_0^{2\pi} d\phi f_{P_j} \sigma_{P_j} G(v_{P_j}/\sigma_{P_j}), \quad (21)$$

where

$$G(x) = \sqrt{\frac{\pi}{8}} e^{-x^2/4} [(2+x^2)I_0(x^2/4) + x^2 I_1(x^2/4)] \quad (22)$$

and I_ν is the modified Bessel function of order ν .

The combination $\sigma_{P_j} G(v_{P_j}/\sigma_{P_j})$ is the result of the integration on the velocity distribution, again assumed to be a gaussian with dispersion σ_{P_j} centered on the rotation velocity v_{P_j} . For further details on this point, see the appendix of Alexander & Sternberg (1999).

The function $G(x)$ satisfies the following limits

$$\lim_{v_{P_j} \rightarrow 0} \sigma_{P_j} G(v_{P_j}/\sigma_{P_j}) = \sqrt{\pi/2} \sigma_{P_j} \quad (23)$$

$$\lim_{\sigma_{P_j} \rightarrow 0} \sigma_{P_j} G(v_{P_j}/\sigma_{P_j}) = v_{P_j}. \quad (24)$$

Applying equation (21) to each of our four populations, we obtain the curves in Figure 14. We see that the more distant populations move more slowly and thus generate new events at a lower rate. For this reason the rate of the bulge events practically coincides with the rate of P1+P2, while the rate of the disk drops to levels comparable to those of P3.

Having calculated both the rate and the number of simultaneously present events, we immediately derive the average time spent by an event above threshold as

$$\langle \Delta T_{P_j} \rangle = \frac{N_{P_j}}{\Gamma_{P_j}} \simeq \frac{\pi \langle R_Z \rangle}{2 \langle v_{\perp} \rangle}, \quad (25)$$

where the last equality holds approximatively and involves the average radius of the lensing zone $\langle R_Z \rangle$, and the average transverse velocity $\langle v_{\perp} \rangle$.

The average duration of the events for each source population are drawn in Figure 15. It grows with the chosen threshold of the experiment. This is due to the fact that as K_{thr} is increased the lensing zone becomes larger and larger and the time required by the sources to cross it becomes proportionally larger (see the approximate expression in eq. [25]).

The modulation in the growth at intermediate thresholds in the K -band is again an effect of the presence of different stellar branches in each population. In fact, at low K_{thr} most of the events are due to bright sources in the red clump. Given their intrinsic luminosity, these sources generate secondary images that stay longer above threshold. At intermediate thresholds, there emerges a non-negligible contribution from fainter sources. These sources have a smaller lensing zone and their secondary images spend much less time above threshold with respect to the brighter sources. The distribution of the average duration becomes bimodal, with the brighter sources enjoying a long time above threshold and the fainter sources spending less time above threshold. The average time of such a bimodal distribution is therefore in the middle between the two maxima. As we increase K_{thr} further, the fainter sources dominate with respect to the brighter and ΔT_{P_j} is determined by these sources only. Then the modulation observed at intermediate K_{thr} in the curves in Figure 15 is just the transition from a regime dominated by more luminous sources to a regime dominated by dimmer sources. In the V -band this transition is less evident.

Coming to a quantitative analysis of the average duration, we note that the events involving sources in the disk of M31 last up to several centuries. For the bulge the average time spent above threshold ranges from 50 to 200 years. For P1+P2 the situation is more dynamical, thanks to the higher velocities characterizing the stars very close to the central black hole. An observational campaign lasting several years could study the evolution of the secondary images already present and hope to see new events (if the threshold magnitude is sufficiently high). The average duration of the events involving sources in P3 is of the order

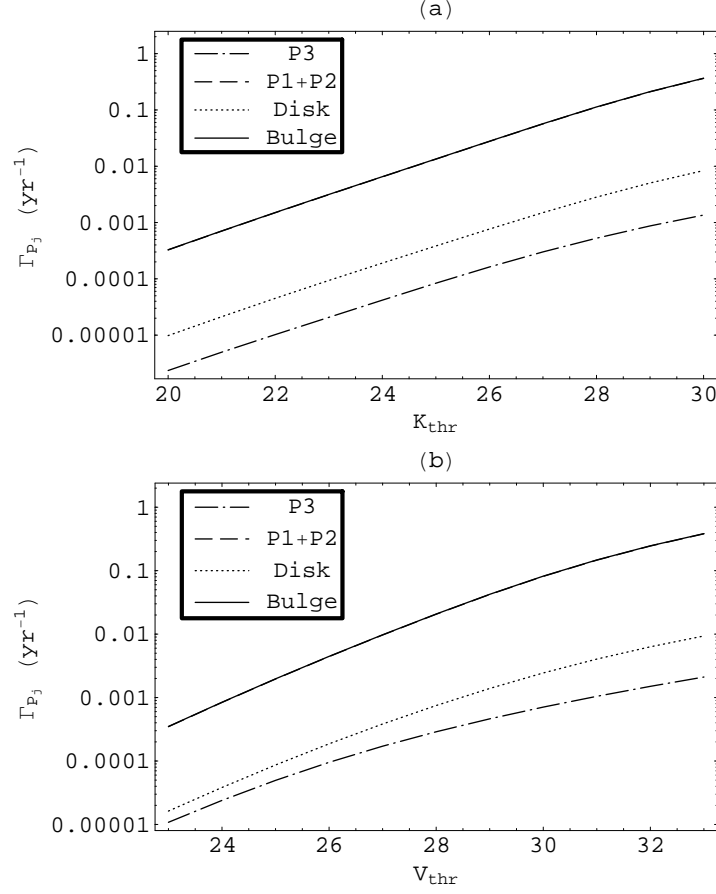


Fig. 14.— (a) Rate of the gravitational lensing events for the four source populations considered in the text expected in the K -band as function of the threshold magnitude. (b) The same in the V -band. The rate of P1+P2 and the rate of the bulge practically coincide.

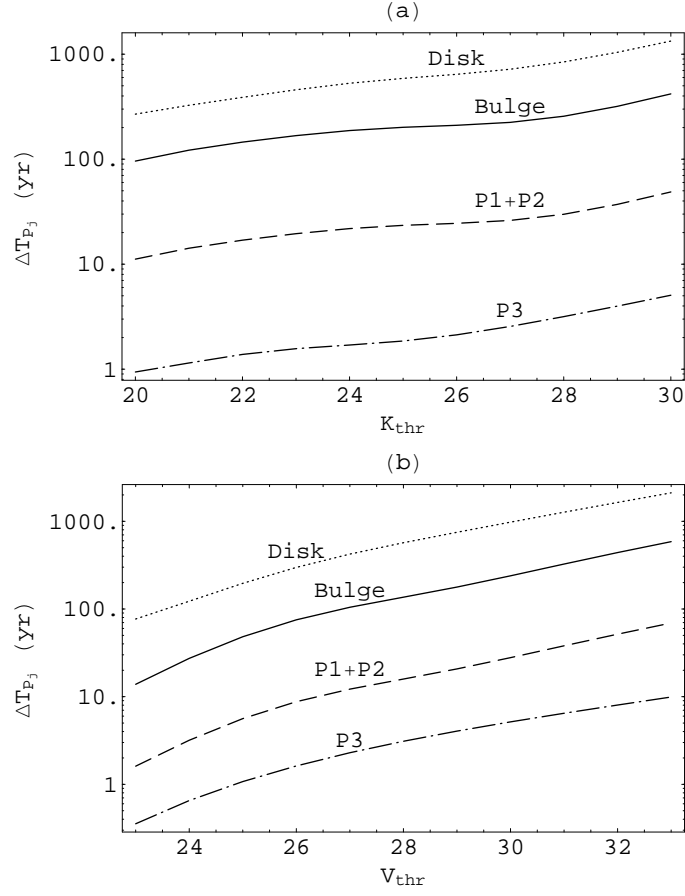


Fig. 15.— (a) Average time spent above threshold in the K -band for the gravitational lensing events for the four source populations. (b) The same in the V -band.

of one year, but the extremely low rate of new events for this population leads one to discard it as a source of gravitational lensing events.

10. Identification of the lensing images

On the basis of the analysis given in the previous sections, it is time to set up a realistic methodology to select the candidate lensing images and test their authenticity.

As mentioned before, the most probable lensing events will involve bulge stars as sources, at typical distances ranging from a few pc to 1 kpc from the lens. In this configuration, the secondary images may form at an angular distance from the central black hole ranging from a few mas to $0.1''$. In order to get access to the bulk of the gravitational lensing events, it is then mandatory to employ interferometry. At this point, the question arises whether a secondary image of a lensed star can be distinguished from a background star unambiguously.

In this respect, it is instructive to calculate the expected number of background stars in an angular area within radius θ centered on the black hole. For a threshold magnitude K_{thr} , only the sources with observed magnitude $K < K_{\text{thr}}$ will be observable. This fixes a threshold on the intrinsic magnitude of the sources as

$$M_{K,\text{max}} = K_{\text{thr}} - 5 \log_{10} \frac{D_{\text{Os}}}{10 \text{ pc}} - A_K. \quad (26)$$

The number of background sources is then

$$B_{P_j}(K_{\text{thr}}, \theta) = \int_{-\infty}^{M_{K,\text{max}}} dM_K n_{P_j}(M_K) \int_{-D_{\text{OL}}}^{\infty} dz \int_0^{\theta(z+D_{\text{OL}})} dr r \int_0^{2\pi} d\phi f_{P_j}(z, r, \phi). \quad (27)$$

Actually, since the spatial distributions for all source populations are centered on the black hole and have an extent much smaller than D_{OL} , we can take the approximation $z \ll D_{\text{OL}}$ and push the lower extremum in the z -integral to $-\infty$.

Let us imagine an observational campaign to discover secondary images due to gravitational lensing lying within $\theta = 0.01''$ of the central black hole. Fixing $K_{\text{thr}} = 24$, the number of background stars in such area is $B_{P_3} = 3.5 \times 10^{-2}$, $B_{P_1+P_2} = 8.3$, $B_{\text{Bulge}} = 3.7$, $B_{\text{Disk}} = 1.1 \times 10^{-2}$.

Our image will thus contain something like 12 stars within $0.01''$ from the central black hole. The first step would be to check for possible alignments between these stars and the

central black hole. If we find that the line joining two stars passes through the central black hole, we can select these stars as candidate lensing images of the same source. Since gravitational lensing is an achromatic phenomenon, the two images must have the same color indices (unless there is reason to believe that the photon paths of the two images cross regions with sensibly different amount of dust). Therefore, false candidates could be excluded taking images in different IR bands and checking whether the luminosity ratio between the two images remains the same in all bands.

A further test is to take another image after several months or even the next year. If the alignment is just a chance product and one of the two stars has a high enough proper motion (which is likely to happen if the star is intrinsically close to the central black hole), then the alignment will be lost in the second image. Conversely, if the alignment is an authentic product of gravitational lensing, and if any evolution shows up, then the two images must move in such a way that the line joining them always passes through the black hole. However, as shown in § 8, the proper motion of the secondary images is typically below 0.1 mas/y. Therefore, it would be improbable that the observed events show any evolution within less than ten years. Moreover, given the very low rate of new events, follow-up observations would make sense only if thresholds higher than $K_{\text{thr}} = 30$ are reached in the observations.

Our estimate of 12 background stars in an area of radius 0.01'' centered on the black hole is based on our spatial distributions, which do not take into account a possible presence of a further cuspy cluster of stars internal to P3 and thus very close to the supermassive black hole. If such a cluster were present, then the number of background stars would sensibly increase. However, these stars would move very fast and chance alignments in a first image would be easily discarded after the analysis of a second image. As stressed before, the most delicate background actually comes from stars that lie along the line of sight but intrinsically far from the black hole and consequently have slow proper motion. We believe that the number of these stars is correctly estimated through equation (27). For completeness, we also mention that the estimate of background stars for $K_{\text{thr}} = 30$ yields 1600 stars and for $V_{\text{thr}} = 33$ gives 1320 stars.

As a final consideration, we note that the deformation of the point-like image of the source is of the order of 10^{-7} arcsec for the gravitational lensing events considered in this work. This prevents from using image deformation as a selection tool for lensing effects.

11. Conclusions

In this paper we have undertaken a deep investigation of the possible observation of gravitational lensing effects due to the black hole in the center of M31. We have considered stars belonging to four different populations (bulge, disk and the central clusters P1+P2 and P3) as candidate sources. Through detailed modelling of the spatial distributions and the luminosity functions of these four populations we have calculated several quantities that can be used to quantify the power of the central black hole as a gravitational lens using present and future observational facilities. We have carried out our analysis both in the K -band and in the V -band.

The main outcome is the number of expected lensed sources at a given time whose secondary image is brighter than a specified threshold magnitude. The results are summarized in Figure 6 and Tables 3 and 4, showing that indeed we expect 1.4 lensed sources at a threshold $K_{\text{thr}} = 24$, 16 events at $K_{\text{thr}} = 27$ and 180 events at $K_{\text{thr}} = 30$. In the V -band we would have 1.3 events at $V_{\text{thr}} = 27$, 25 events at $V_{\text{thr}} = 30$ and 270 events at $V_{\text{thr}} = 33$.

We have also presented the distribution of the lensed sources as a function of their absolute magnitude, showing the contribution of different stellar branches as sources of gravitational lensing events.

The distribution of the lensed sources as a function of the distance shows that the disk stars are mostly lensed at about 1 kpc distance from the black hole, whereas the bulge stars can be lensed at distances ranging from a few pc to 1 kpc. The inner cluster stars are lensed at fractions of a pc.

This difference is reflected in the angular separation of the images from the black hole, which ranges from 1 mas to $0.1''$ for bulge and disk stars, whereas it stays of the order 1 mas or below for the inner clusters. The resolution needed to get a significant number of events is thus of the order of a few mas, requiring the employment of long baseline interferometers or extremely large telescopes. This justifies our choice to present our analysis in the K -band, for which the present infrared interferometers such as Keck, LBT and the future space telescope JWST are optimized. The VLTI, though representing the most advanced interferometer operating in IR bands, cannot observe M31 efficiently. The parallel analysis in the V -band provides a deeper comprehension of all the effects coming into play. In this band, the expectations for the number of lensing events are comparable to those in the K -band, provided that V -band interferometers are constructed in the future with sizes of the same order as in the K -band.

The gravitational lensing events discussed in this paper have a very slow evolution, with typical angular velocities of the images between 0.01 and 0.1 mas/y. We have outlined

a possible observational strategy to select gravitational lensing events within the expected background stars, by checking the alignment of pairs of images, the achromaticity of the flux ratio and setting up follow-up observations to detect any secular development.

Our analysis can be repeated with different models of the source populations. Given the present uncertainties on the morphology of the components of M31, we believe that our estimates can be corrected by a factor of a few at most.

The chances for concrete observations of gravitational lensing events by the supermassive black hole in M31 are rather low (though not null) even with the best facilities available today. The perspectives will be definitely increased with the realization of future projects such as the JWST, the extremely large ground telescopes or the realization of new long baseline optical interferometers in the northern hemisphere. With such facilities it should be possible to reach the higher thresholds indicated in this paper while keeping a very high angular resolution. This would open the way to an intensive research of gravitational lensing events and to their use in the investigation of the environment of the supermassive black hole.

We are grateful to Gaetano Scarpetta and an anonymous referee for some fundamental comments which have taken to a consistent improvement of the manuscript. This work has made use of the IAC-STAR Synthetic CMD computation code. IAC-STAR is supported and maintained by the computer division of the Instituto de Astrofísica de Canarias. The authors acknowledge support for this work by MIUR through PRIN 2006 Prot. 2006023491_003 and by research funds of the Salerno University.

REFERENCES

- Alexander, T. 2001, *ApJ*, 553, L149
- Alexander, T., & Loeb, A. 2001, *ApJ*, 551, 223
- Alexander, T., & Sternberg, A. 1999, *ApJ*, 520, 137
- Aparicio, A., & Gallart, C. 2004, *AJ*, 128, 1465
- Bellazzini, M., Cacciari, C., Federici, L., et al. 2003, *A&A*, 405, 867
- Bender, R., Kormendy, J., Bower, G., et al. 2005, *ApJ*, 631, 280
- Bozza, V. 2002, *Phys. Rev. D*, 66, 103001

- Bozza, V. & Mancini, L. 2004, *ApJ*, 611, 1045
- Bozza, V. & Mancini, L. 2005, *ApJ*, 627, 790
- Chanamé, J., Gould, A., & Miralda-Escudé, J. 2001, *ApJ*, 563, 793
- Chang, Ph., Murray-Clay, R., Chiang, E., & Quataert, E. 2007, *ApJ*, 668, 236
- Cox, A.N. 2001, *Allen’s Astrophysical quantities*, New York, Springer
- Darwin, C. 1959, *Proc. of the Royal Soc. of London A*, 249, 180
- De Paolis, F., Geralico, A., Ingrosso, G., & Nucita, A.A. 2003, *A&A*, 409, 809
- Demarque, P., & Virani, S., 2007, *A&A*, 461, 651
- Eckart, A., & Genzel, R. 1997, *MNRAS*, 284, 576
- Eckart, A., Genzel, R., Ott, T., & Schödel, R. 2002, *MNRAS*, 331, 917
- Eisenhauer, F., Genzel, R., Alexander, T., et al. 2005, *ApJ*, 628, 246
- Gardner, J.P., Mather, J.C., Clampin, M., et al. 2006, *Space Science Reviews*, 123, 485
- Genzel, R., Thatte, N., Krabbe, A., et al. 1996, *ApJ*, 472, 153
- Ghez, A.M., Klein, B.L., Morris, M., & Becklin, E.E. 1998, *ApJ*, 509, 678
- Ghez, A.M., Duchêne, G., Matthews, K., et al. 2003, *ApJ*, 586, L127
- Ghez, A.M., Salim, S., Hornstein, et al. 2005, *ApJ*, 620, 744
- Han, C. 1996, *ApJ*, 472, 108
- Hodge, P. 1989, *ARA&A*, 27, 139
- Jaroszyński, M., 1998, *Acta Astron.*, 48, 413
- Keeton, C.R., & Petters, A.O. 2005, *Phys. Rev. D*, 72, 104006
- Kent, S.M. 1989, *AJ*, 97, 1614
- King, I.R., Stanford, S.A., & Crane, P. 1995, *AJ*, 109, 164
- Kochanek, C.S., Schneider, P., & Wambsganss, J. 2004, *Proceedings of the 33rd Saas-Fee Advanced Course*, G. Meylan, P. Jetzer & P. North, eds. (Springer-Verlag: Berlin)

- Kroupa, P., Tout, C.A., & Gilmore, G. 1993, MNRAS, 262, 545
- Lauer, T.R., Faber, S.M., Groth, E.J., et al. 1993, AJ, 106, 1436
- Nusser, A., & Broadhurst, T. 2004, MNRAS, 355, L6
- Olsen, K.A.G., Blum, R.D., Stephens, A.W., et al. 2006, AJ, 132, 271
- Paumard, T., Genzel R., Martins, F., et al. 2006, ApJ, 643, 1011
- Peiris, H.V., & Tremaine, S. 2003, ApJ, 599, 237
- Reid, M.J., Menten, K.M., Trippe, S., et al. 2006, ApJ, 659, 378
- Sarajedini, A., & Jablonka, P. 2005, AJ, 130, 1627
- Schlegel, D.J., Finkbeiner, D.P., & Davis, M. 1998, ApJ, 500, 525
- Schödel, R., Ott, T., Genzel, R., et al. 2002, Nature, 419, 694
- Schödel, R., Ott, T., Genzel, R., et al. 2003, ApJ, 596, 1015
- Schwarzschild, M., 1979, ApJ, 232, 236
- Tremaine, S., 1995, AJ, 110, 628
- Virbhadra, K.S., & Ellis, G.F.R. 2000, Phys. Rev. D, 62, 084003
- Wardle, M., & Yusuf-Zadeh, F. 1992, ApJ, 387, L65
- Weinberg, N.N., Milosavljevic, M., & Ghez, A.M. 2005, ASP Conf. Proc. 338, 252
- Widrow, L.M., & Dubinski, J., 2005, ApJ, 631, 838
- Williams, B.F., 2002, MNRAS, 331, 293